Journal of Colloid and Interface Science **224,** 408–416 (2000)
doi:10.1006/jcis.2000.6737, available online at http://www.idealibrary.com on IDEAL®

Local Structure Analysis of Strontium Sorption to Hydrous Manganese Oxide

L. Axe,[1,*] T. Tyson,† P. Trivedi,* and T. Morrison‡

*Department of Civil and Environmental Engineering and †Department of Physics, New Jersey Institute of Technology, Newark, New Jersey 07102; and ‡Department of Physics, Illinois Institute of Technology, Chicago, Illinois 60616

E-mail: axe@adm.njit.edu

Received October 4, 1999; accepted January 18, 2000

To develop mechanistic models of contaminant distribution processes, we conducted an X-ray absorption fine structure analysis of strontium sorption to hydrous manganese oxide (HMO). Sr *K*-edge measurements were performed at 298, 220, and 77 K, and at sample loadings from 10^{-4} to 10^{-2} mol Sr/g HMO. Results from fitting the first shell in the sorbed samples indicate that strontium is surrounded by 10–12 oxygen atoms at an average distance of 2.58 Å. This coordination environment is consistent with the strontium atom remaining hydrated upon sorption to the oxide, where in water hydrated strontium has approximately 9 atoms of oxygen at 2.62 Å. Furthermore, the temperature dependence of the strontium–oxygen bond also suggests physical adsorption due to the large contribution of the dynamic component of the Debye Waller factor. Although second-shell data are consistent with either 3 manganese atoms at 4.12 Å or 6 strontium atoms at 3.88 Å, both the near-edge and fine structure data for the manganese *K*-edge indicate that the local coordination environment of the manganese ion remains intact as a function of time or strontium sorption. Furthermore, the local structure of amorphous manganese oxide is highly ordered.

Key Words: **XAS; manganese oxide; strontium; sorption.**

INTRODUCTION

X-ray absorption spectroscopy (XAS) is a noninvasive tool for probing the local coordination environment of a contaminant *in situ.* Both the extended X-ray absorption fine structure (XAFS) and the near-edge spectra (XANES) have been employed environmentally in well-defined model systems and in more complex contaminated soils and sediments (1–11). In this research, we have studied the local coordination environment of strontium sorption to hydrous manganese oxide. Strontium 90 is a recognized carcinogen that is a concern due to its release into the environment from nuclear wastes. Therefore, it is important to understand the distribution mechanisms and mobility of strontium released in soils and sediments. The results presented here are compared to earlier work where we considered sorption to hydrous iron oxide (7).

Amorphous aluminum, iron, and manganese oxides are prevalent in soils and sediments. These hydrous oxides act as sinks and sources for metal contaminants (11–15) due to their porous structures, great capacity for metals, and presence as both coatings and discrete particles. Recent XAS studies (7) of strontium sorption to hydrous iron oxide (HFO) revealed that the local coordination environment for strontium is highly disordered, and Gaussian distributions for one or two subshells could not describe the distribution of atoms. The cumulant expansion proved to be effective for describing the distribution of first- and second-shell neighbors. For small disorder, where $k_{\max}\sigma \ll 1$ (where k is the wave number and σ^2 is the mean square disorder), higher order cumulants can be neglected, and the distribution can be described as Gaussian. However, third and fourth moments are useful for non-Gaussian distributions, when moderate disorder exists (7, 16, 17). Even and odd cumulants define the amplitude and phase, respectively. The mean, $C_1 = R$, and the variance, $C_2 = \sigma^2$, are both positive, while C_3 and C_4 measure skewing and weight in the tails of the distribution, respectively, and can be either positive or negative. Axe *et al.* (7) observed disorder in the first shell of references used in their study despite, for example, the long-range order, crystallinity, in one reference, SrO. In the sorption samples, they found the first-shell environment to be consistent with the strontium ion remaining hydrated, thus indicating a physical type of adsorption. Interestingly, Collins *et al.* (18) observed different mechanisms for strontium sorption to goethite as a function of pH. At a pH of 10.2, they established second-shell contributions from iron on the goethite surface. In their analysis, two waters of hydration were lost upon adsorption, with an overall fit of 8 oxygen atoms suggesting that 2 oxygen atoms from the goethite surface contributed to the first shell. As the pH decreases and the net surface charge decreases, Collins *et al.* found outer-sphere complexation at a pH of 9.2. Chen *et al.* (19) also found an outer-sphere complex formation for strontium sorption to a variety of clays, where the coordination environment for the first shell was invariant of the specific clay, pH, and ionic strength. In a similar study, Parkman *et al.*

[1] To whom correspondence should be addressed.

0021-9797/00 $35.00

(20) assessed strontium sorption to calcite and kaolinite using XANES and XAFS. They proposed that in their lower loadings of strontium on calcite, ion exchange occurs on the surface where half of the environment is that of the calcite and the other is of solvation, explaining both their XANES and XAFS results. At higher loadings, they concluded that strontium precipitated as a poorly ordered strontianite. On the other hand, for strontium sorption to kaolinite Parkman *et al.* observed only first-shell contributions. They found approximately 9 oxygen atoms in the first shell, which was attributed to strontium bonding with waters of hydration as well as adsorbing on the surface.

Manceau and co-workers have studied the local coordination environment of both hydrous iron and manganese oxides with XAS (1, 2, 21–24). They have found that in contrast to hydrous iron oxide (HFO), where interpolyhedral linkages typical of well-crystallized Fe minerals were present in the premineral gel, Mn^{4+} gels appeared to have a more random framework of edge- and corner-sharing MnO_2 octahedra, and these were not strictly related to well-crystallized Mn minerals. Manceau *et al.* (2) noted that the differences between HFO and HMO could explain why HMO can develop into so many types of minerals. In this research, the stability and local coordination environment of Mn is important in understanding Sr sorption and mobility.

METHODS

Hydrous manganese oxide was precipitated using the method of Gadde and Laitinen (25), where manganese(II) nitrate solution was slowly added to alkaline sodium permanganate solution. The amounts of manganese(II) nitrate, sodium permanganate, and sodium hydroxide mixed were in the mole ratio 3 : 2 : 4. The suspension was aged for 4 h and then centrifuged and rinsed. Methods used for characterizing the amorphous oxide included the BET (Brunauer–Emmett–Teller) method for measuring surface area, potentiometric titration for estimating the pH zero point of charge, sorption studies for finding site density, nitrogen desorption for determining the pore size distribution (micro-, meso-, and/or macro-pores), particle counting for the particle size distribution, X-ray diffraction for assessing crystallinity (or lack of), environmental scanning electron microscopy (ESEM) with energy dispersive X-ray (EDX) analysis for studying shape and surface composition, and XAS for obtaining local structural information. X-ray diffraction was also used to assess the manganese oxide mineralogy as a function of time with and without Sr present. These tests were conducted to assess whether contaminant sorption influences the aging of HMO to crystalline minerals.

XAS

X-ray absorption fine structure spectroscopy was conducted at NSLS beamline X11A. The storage ring operates at 2.528 and 2.8 GeV with a typical current of approximately 200 mA. Monochromatic radiation was achieved with Si(111) crystals. The strontium K-edge absorption data (both samples and standards) were collected in transmission mode with nitrogen gas in the ion chamber before the sample (I_0) and with argon gas in the ion chamber after the sample (I_t). XAFS spectra were collected on the Sr K-edge over the energy range 15,960–16,965 eV. A Displex (Advanced Research Systems) with an evacuated sample chamber was used for studies conducted at 77 and 200 K. Suspensions were placed in aluminum cells (except the solution which was set in an acrylic holder) and sealed with epoxy and Kapton windows. Manganese K alpha fluorescence X-rays were measured with a Stern–Heald type fluorescence ionization chamber utilizing argon. Samples were positioned 45° to the incident radiation beam with a Cr ($Z-1$) filter and Soller slits positioned between the sample and detector. Data were collected over the energy range 6,300–7,600 eV. Harmonic rejection was achieved by detuning the monochromator to 80% of fully tuned I_0.

Adsorption samples were prepared in batch reactors at room temperature (∼22° C). The ionic strength was maintained at 3×10^{-2} using sodium nitrate as the background electrolyte. Sample equilibration time for adsorption studies and HMO samples without the sorbate strontium ranged from 4 h to 6 months. All suspensions were maintained at pH 7 with Sr loadings ranging from 10^{-4} to 10^{-2} mol Sr per gram or 2.8×10^{-7} to 2.8×10^{-5} mol Sr per m^2 of HMO. Thermodynamically the strontium concentrations used in these samples were below saturation with respect to $SrCO_3$ (26).

Reference samples included a 0.05 molar solution of strontium nitrate in deionized water, and crystalline strontium oxide and strontium carbonate of known structures. The oxide and carbonate were purchased from Aldrich Chemical, and X-ray diffraction (XRD) patterns were confirmed using a Philips X'Pert-MPD XRD System. No well-characterized Sr–Mn compounds were available for this study.

Sample thickness for fluorescence measurements of Mn in the HMO paste (no sample drying over the course of data collection) was approximately 3 mm. The Sr–HMO samples, SrO, $SrCO_3$, and 0.05 M Sr were measured in transmission.

Data Analyses

The reduction of the XAFS data was performed with the MacXAFS4.1 (27) package using standard procedures (28) as recently applied to Sr sorption to HFO (7). The photoelectron momentum was defined in the normal way, $k = ((2m/\hbar^2)(E - E_0))^{1/2}$, where $\hbar$ is Plank's constant. Normalization of the data was carried out by defining a first-order polynomial fit in the pre-edge region to zero and a third-order polynomial fit over the region above the edge to unity at E_0. For each sample, XAFS was extracted from the spectrum as the difference between the normalized spectrum and an adjustable spline function fit through the post-edge region; the parameters were adjusted to minimize the area under the curve for the region $r < 1$ Å of the Fourier transform without reducing the amplitude of the first-shell peak. Peaks in this region for hydrated strontium

have been shown (29) to result from multielectron excitation effects. However, on the scale of our analysis, contributions from multielectron excitations are negligible (29).

In performing the fits, the amplitudes, S_0^2, were defined by fitting the spectrum of the strontium oxide model compound. The errors in the structural parameters were computed based on the stability of the fits. For disordered shells, the distributions were modeled using the more general cumulant expansion method (7, 16, 17). Model scattering amplitudes and phases were computed using the code FEFF7 (30).

RESULTS AND DISCUSSION

HMO Characteristics

The surface area and the pore size radii (bimodal) of freeze-dried HMO were evaluated with the BET and nitrogen desorption methods and were found to be 359 m^2/g and 2.1 and 6.1 nm, respectively. The spherical, aggregated HMO particles ranged from 1 to 150 μm with a zero point of charge of 2.55 ± 0.05; these results are in agreement with other studies (31–33). The shape of the hydrated and centrifuged HMO was evaluated with the ESEM; aggregated particles were generally spherical with highly irregular topography. Also, using the ESEM, no differences were observed between samples with and without Sr sorbed. Furthermore, using EDX to map the surfaces, Sr was uniformly distributed.

To test the hypothesis that crystallization of HMO is inhibited due to the presence of contaminants, XRD was used to measure macroscopic variations in oxide aging (i.e., freshly precipitated, 3 months, and 6 months) after formation as a function of contaminant loading. The XRD pattern was broad and flat, representative of amorphous manganese oxide (Fig. 1). The pattern is consistent up to the duration of the study, 6 months. Furthermore, with an Sr loading of 10^{-2} mol per gram of HMO, the XRD patterns are invariable, where the oxide remains amorphous and there is no evidence of an Sr precipitate.

XAS Studies

Room-temperature data reduced to $\chi(k) \cdot k^3$ versus k are presented in Fig. 2 for the sorbed samples of 10^{-4} to 10^{-2} mol Sr per gram of HMO and standards of SrO, $SrCO_3$, and aqueous strontium nitrate solution. These data were filtered over the range 2.0 to 12.3 $Å^{-1}$ (except for the data with 10^{-3} mol Sr sorbed that was filtered over the range 2.0 to 10.5 $Å^{-1}$); the Fourier transform versus radial coordinate is shown as amplitude and imaginary part in Figs. 3 and 4. The radial coordinate (Å) is not the true radial distance as it is not corrected for the phase shift. In addition, Fig. 4 includes $SrCO_3$ collected at 77 K; as the temperature decreases the thermal component of the Debye Waller factor (mean square variation of distances) decreases, resulting in an increase in magnitude for both first- and second-shell contributions.

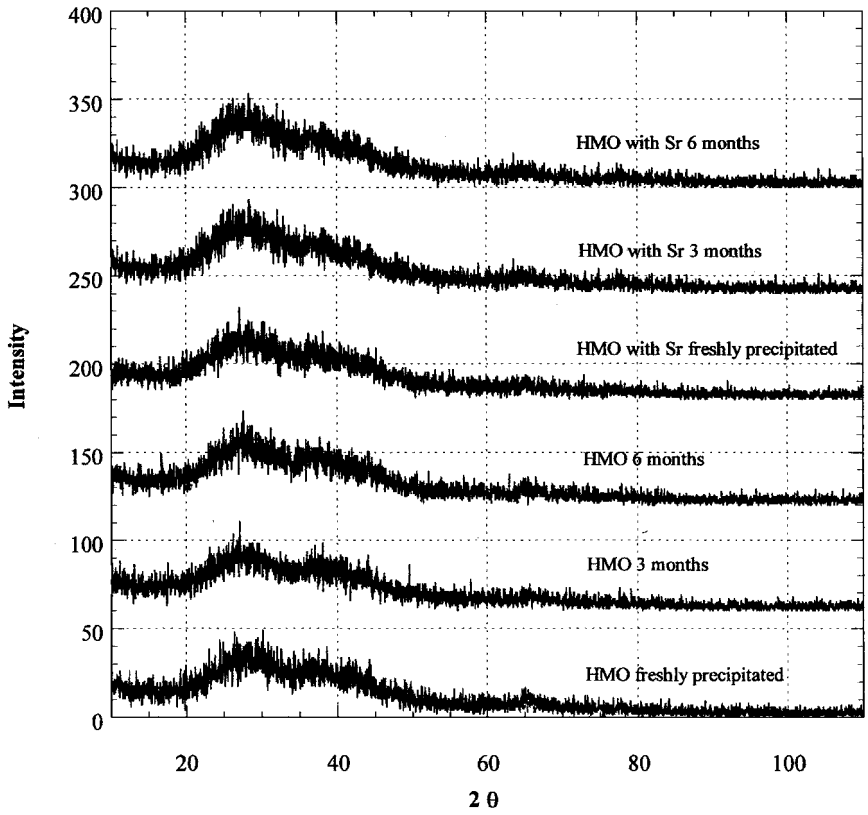

FIG. 1. X-ray diffraction of hydrous manganese oxide as a function of time with and without strontium.

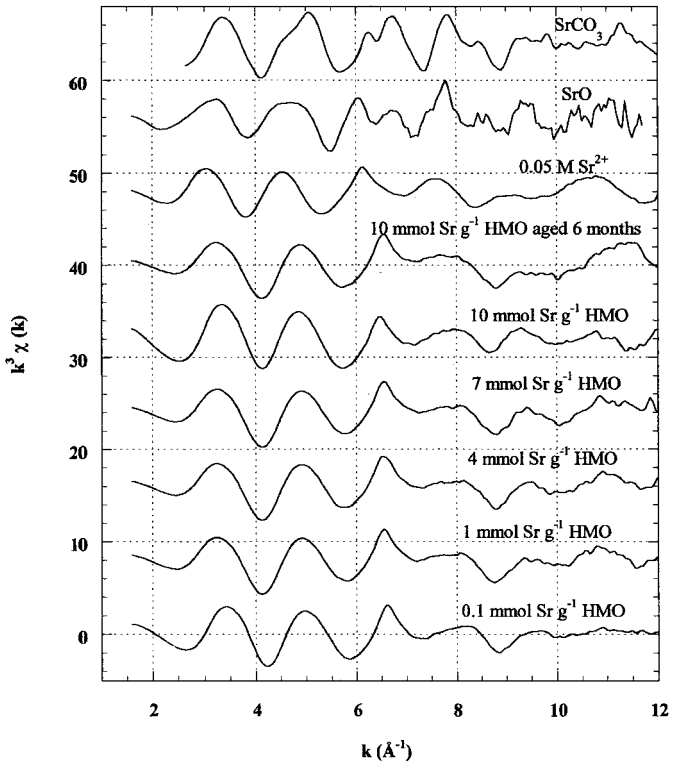

FIG. 2. Sr *K*-edge data reduced to $\chi(k) \cdot k^3$ versus k at 298 K.

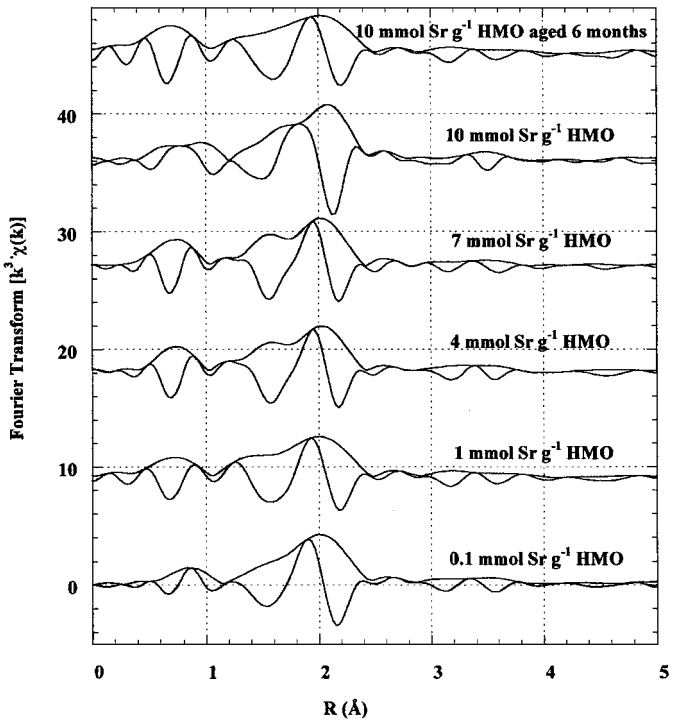

FIG. 3. Fourier transform $[k^3 \cdot \chi(k)]$ versus radial coordinate filtered from 2.0 to 12.3 Å^{-1}, except for the 0.1 mmol Sr g^{-1} HMO loading, which was filtered from 2.0 to 10.5 Å^{-1}.

Fitting was conducted on the inverse Fourier transform window for first-shell and subsequent multishell fits; second-shell contributions could not be isolated due to spectra leakage from the first shell. In all fits, no parameter was constrained or fixed other than the edge energy, which was constrained to being equivalent for all shells in the fit. For sorbed samples, the two shells were fitted over a radial window of 1.1 to 3.9 Å. Using a Gaussian model with single and multiple shells resulted in poor fits for standards and samples. Fits were subsequently conducted including the third and fourth cumulants to help describe the distribution of atoms in a shell. The best, multishell fits are presented in Table 1, and a representative fit is shown in Fig. 5; all fits were within the noise of the data, which refers to the multiple scans used in averaging the normalized data. In these multishell fits, the first shell results were equivalent to fits from isolating the first shell, where the strontium ion was found to be surrounded by approximately 10 to 12 oxygen atoms at about 2.58 Å . In earlier work, Axe *et al.* (7) found a similar environment for the first shell when strontium sorbs to HFO. Comparing this first-shell distribution to SrO, aqueous strontium nitrate, and $SrCO_3$ references (Table 2), the sorbed samples do not correspond well with the powder references. Although strontium carbonate is the most thermodynamically stable solid when strontium concentrations exceed saturation (26), first-shell distances for the sorbed samples are not consistent with that of the carbonate. Furthermore, strontium carbonate has a broad range of second-shell contributions (non-Gaussian distribution) that include both oxygen and

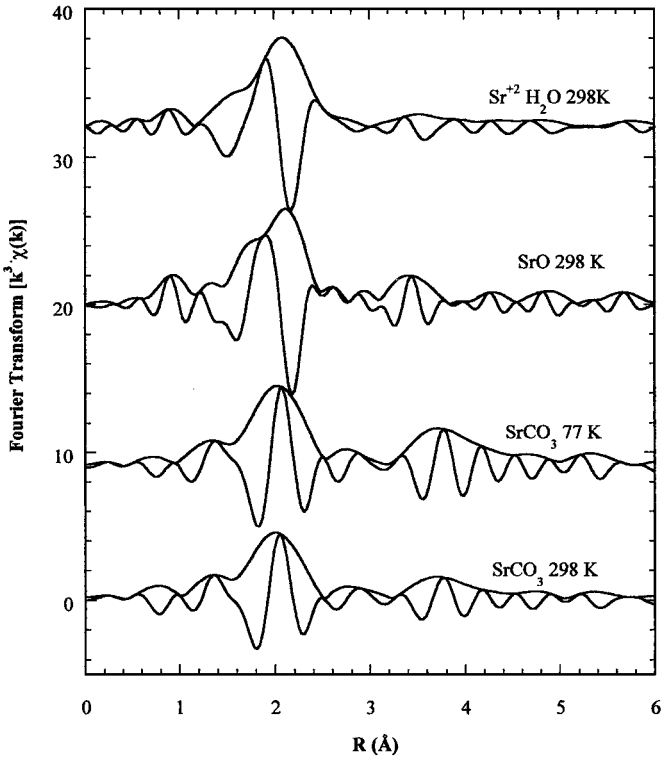

FIG. 4. Fourier transform $[k^3 \cdot \chi(k)]$ versus radial coordinate filtered from 2.4 to 11.5 Å^{-1}.

TABLE 1

First (Oxygen)- and Second-Shell Best Fits for Sr *K*-Edge Data at 298 K, *k*-Range 2.0 to 12.3 Å^{-1} and *r*-Range 1.1 to 3.9 Å

	Sample	Res. (%)	N_1	R_1 (Å)	σ_1^2 (Å^2)	$C_{3,1}$ (Å^3)	$C_{4,1}$
1.	1×10^{-4} mol Sr g^{-1} (Mn)[a]	1.06	9.54 ± 5.79	2.61 ± 0.10	0.012 ± 0.017	5.5e-4 ± 2.0e-3	−9.0e-6 ± 5.6e-4
2.	1×10^{-4} mol Sr g^{-1} (Sr)	1.31	9.97 ± 5.93	2.61 ± 0.11	0.013 ± 0.016	5.9e-4 ± 2.0e-3	−9.0e-6 ± 2.3e-3
3.	1×10^{-3} mol Sr g^{-1} (Mn)	1.86	12.79 ± 12.13	2.54 ± 0.13	0.020 ± 0.024	−7.4e-4 ± 2.4e-3	−2.3e-4 ± 7.9e-4
4.	1×10^{-3} mol Sr g^{-1} (Sr)	1.93	14.10 ± 12.93	2.53 ± 0.14	0.023 ± 0.024	−7.8e-4 ± 2.4e-3	−3.0e-4 ± 7.6e-4
5.	4×10^{-3} mol Sr g^{-1} (Mn)	2.27	10.93 ± 5.06	2.57 ± 0.080	0.016 ± 0.012	−1.4e-4 ± 1.3e-3	−1.5e-4 ± 3.2e-4
6.	4×10^{-3} mol Sr g^{-1} (Sr)	2.63	11.19 ± 5.12	2.58 ± 0.069	0.017 ± 0.011	−3.0e-5 ± 1.1e-3	−1.6e-4 ± 3.0e-4
7.	7×10^{-3} mol Sr g^{-1} (Mn)	3.38	11.26 ± 5.58	2.56 ± 0.10	0.017 ± 0.013	−3.9e-4 ± 1.6e-3	−1.7e-4 ± 3.6e-4
8.	7×10^{-3} mol Sr g^{-1} (Sr)	3.77	12.18 ± 6.40	2.57 ± 0.095	0.019 ± 0.013	−1.7e-4 ± 1.5e-3	−2.2e-4 ± 3.8e-4
9.	1×10^{-2} mol Sr g^{-1} (Mn)	0.99	10.83 ± 5.43	2.58 ± 0.079	0.019 ± 0.013	−9.0e-5 ± 1.3e-3	−2.3e-4 ± 3.4e-4
10.	1×10^{-2} mol Sr g^{-1} (Sr)	1.10	11.06 ± 5.57	2.59 ± 0.067	0.019 ± 0.013	1.0e-5 ± 1.0e-3	−2.3e-4 ± 3.4e-4
11.	1×10^{-2} mol Sr g^{-1} aged (Mn)	1.33	10.60 ± 12.70	2.55 ± 0.17	0.014 ± 0.033	−7.3e-4 ± 3.3e-3	4.0e-5 ± 1.1e-3
12.	1×10^{-2} mol Sr g^{-1} aged (Sr)	1.42	12.25 ± 13.63	2.54 ± 0.17	0.018 ± 0.031	−8.1e-4 ± 3.2e-3	−7.5e-5 ± 1.1e-3
			N_2[b]	R_2	σ_2^2	$C_{3,2}$	$C_{4,2}$
1.	1×10^{-4} mol Sr g^{-1} (Mn)[a]		3.70 ± 16.95	4.21 ± 0.23	0.025 ± 0.086	4.1e-3 ± 4.6e-3	−2.8e-4 ± 2.0e-3
2.	1×10^{-4} mol Sr g^{-1} (Sr)		3.63 ± 17.89	3.89 ± 0.24	0.015 ± 0.092	8.5e-4 ± 5.3e-3	9.0e-6 ± 2.3e-3
3.	1×10^{-3} mol Sr g^{-1} (Mn)		2.09 ± 14.73	4.05 ± 0.30	0.015 ± 0.15	8.8e-4 ± 6.8e-3	−3.9e-5 ± 4.2e-3
4.	1×10^{-3} mol Sr g^{-1} (Sr)		6.49 ± 12.54	3.80 ± 0.28	0.026 ± 0.14	−1.3e-3 ± 6.6e-3	−1.7e-4 ± 4.0e-3
5.	4×10^{-3} mol Sr g^{-1} (Mn)		1.52 ± 7.16	4.11 ± 0.19	0.0096 ± 0.078	2.1e-3 ± 3.6e-3	−1.1e-5 ± 1.7e-3
6.	4×10^{-3} mol Sr g^{-1} (Sr)		1.89 ± 13.88	3.93 ± 0.23	0.0089 ± 0.11	1.2e-3 ± 4.6e-3	1.0e-4 ± 2.4e-3
7.	7×10^{-3} mol Sr g^{-1} (Mn)		5.46 ± 21.66	4.14 ± 0.22	0.034 ± 0.073	3.2e-3 ± 3.7e-3	−5.2e-4 ± 1.5e-3
8.	7×10^{-3} mol Sr g^{-1} (Sr)		12.30 ± 56.20	4.00 ± 0.21	0.044 ± 0.07	3.0e-3 ± 2.9e-3	−6.6e-4 ± 1.4e-3
9.	1×10^{-2} mol Sr g^{-1} (Mn)		1.82 ± 9.45	4.13 ± 0.22	0.018 ± 0.087	2.3e-3 ± 4.0e-3	−2.2e-4 ± 1.9e-3
10.	1×10^{-2} mol Sr g^{-1} (Sr)		1.82 ± 9.94	3.86 ± 0.22	0.011 ± 0.086	1.9e-4 ± 4.3e-3	−2.5e-5 ± 1.8e-3
11.	1×10^{-2} mol Sr g^{-1} aged (Mn)		3.93 ± 26.26	4.07 ± 0.31	0.029 ± 0.14	1.3e-3 ± 6.2e-3	−4.4e-4 ± 3.8e-3
12.	1×10^{-2} mol Sr g^{-1} aged (Sr)		10.12 ± 64.40	3.81 ± 0.29	0.036 ± 0.13	−7.6e-4 ± 6.2e-3	−4.6e-4 ± 3.8e-3

[a] (Mn) or (Sr) represents the second-shell atom used in the model.

[b] The significant disorder causes weaker contributions from the higher shells; as a result, the coordination numbers for this second shell have large errors.

carbon, neither of which was observed in the sorbed samples. The highly hydrated strontium system is consistent with the hydrated strontium coordination environment where additional oxygens are due to sorption at the oxide surface. This results in a non-Gaussian distribution as third and fourth cumulants are required to describe the first-shell oxygen distribution. In all but the lowest loading, the mean square variation in distances was greater in the sorbed samples than that for the hydrated strontium solution, which is in agreement with the inclusion of additional first-shell oxygen contributions from the oxide surface. Therefore, these first-shell results suggest that the strontium does not lose its waters of hydration, which were observed in the aqueous strontium nitrate solution. The strontium ion prefers a large number of oxygen atoms (or waters) at multiple distances (which explains a hydrated ion sorbed at the surface) in its first shell. In the second shell, there was no evidence of a lighter element like oxygen, and fitting supports two possible environments, the proximity of a heavier atom of either strontium or manganese for the Sr-loaded HMO of 10^{-4} to 10^{-2} mol g^{-1} at 298 K. Furthermore, the trends in Table 1 suggest that a second shell comprised of Mn resides at approximately 4.12 Å, while that for Sr lies at about 3.88 Å. The significant disorder causes weaker contributions from the higher shells; as a result, the coordination numbers for this second shell have large errors. To resolve the second-shell distribution, temperature studies were conducted as well.

Spectra collected at 77, 200, and 298 K are shown in Fig. 6, where the data have been reduced to $\chi(k) \cdot k^3$ versus k for the samples of 4×10^{-3} and 7×10^{-3} mol Sr per gram HMO. The data were filtered over the range 2.0 to 12.3 Å^{-1} and Fourier

TABLE 2

Best Fits for Hydrated Strontium, SrO, and $SrCO_3$ in the First-Shell *k*-Range 2.4–11.5 Å^{-1} and *r*-Range 1.38–2.80 Å (Except for $SrCO_3$, which was filtered from 2.9–11.5 Å^{-1} and windowed from 0.92 to 2.55 Å)

Sample	Res. (%)	N	R (Å)	σ^2 (Å^2)	C_3 (Å^3)	C_4
SrO	1.0	6.22 ± 1.90	2.60 ± 0.05	0.0096 ± 0.0072	0.0011 ± 0.0007	$-8.6 \times 10^{-5} \pm 1.9 \times 10^{-4}$
Solution	0.2	8.93 ± 1.20	2.62 ± 0.02	0.012 ± 0.004	$8.9 \times 10^{-4} \pm 4.4 \times 10^{-4}$	$-2 \times 10^{-5} \pm 10^{-4}$
$SrCO_3$	2.0	12.96 ± 8.32	2.69 ± 0.11	0.013 ± 0.015	$1.6 \times 10^{-3} \pm 1.8 \times 10^{-3}$	$-9.3 \times 10^{-5} \pm 4.2 \times 10^{-4}$

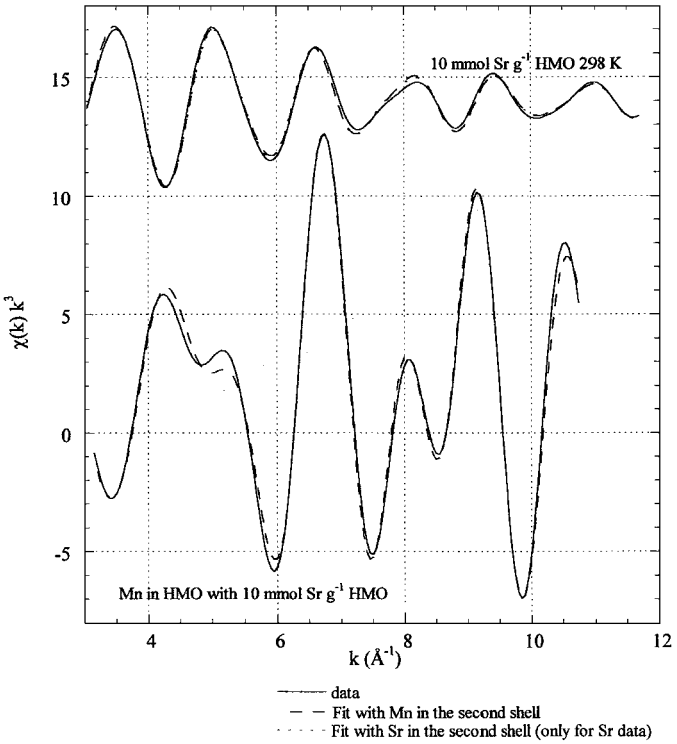

FIG. 5. Representative two-shell fits of inverse Fourier transformed Sr *K*-edge data over 1.1 to 3.9 Å and Mn *K*-edge data over 1.08 to 3.08 Å.

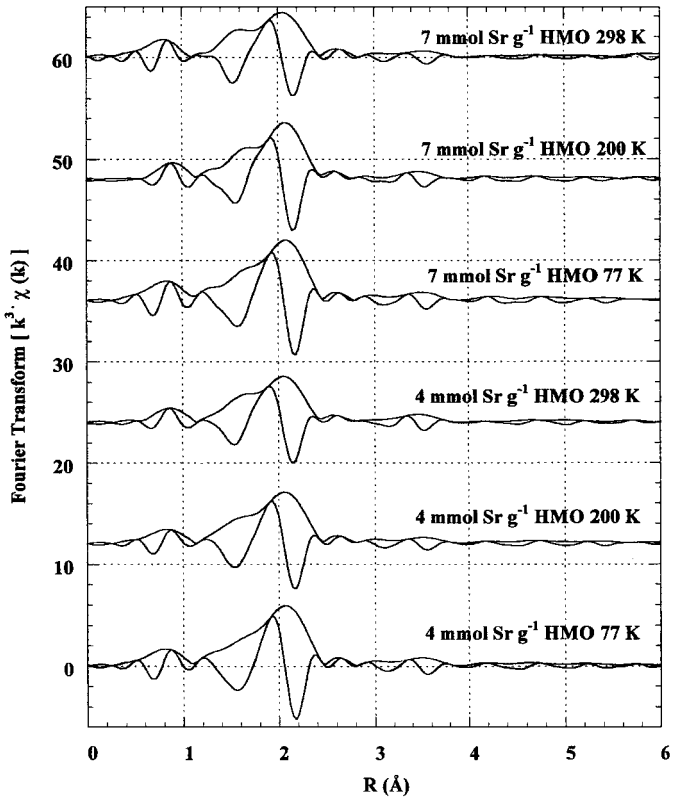

FIG. 7. Fourier transform $[k^3 \cdot \chi(k)]$ versus radial coordinate filtered from 2.0 to 12.3 Å^{-1}.

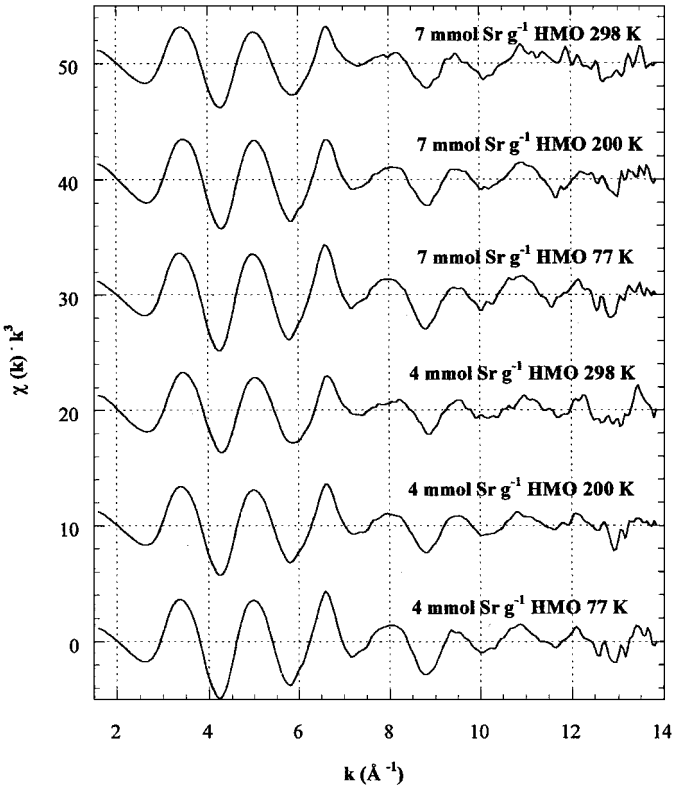

FIG. 6. Sr *K*-edge data reduced to $\chi(k) \cdot k^3$ versus k at 77, 200, and 298 K.

transformed, with the amplitude and imaginary part are shown in Fig. 7. As temperature decreases, the amplitude increases while the mean square variation of distances in the first shell decreases. This effect is detailed in Table 3, where multishell fits are presented (representative fits are shown in Fig. 5). In the first shell, a narrower range of oxygen atoms is observed as compared to the 298 K data presented above; approximately 11 to 12 atoms of oxygen are located at about 2.58 Å . In other words, the first-shell Debye Waller factor decreases with decreasing temperature for the first shell of oxygen atoms, indicating a narrower range.

For the highly disordered sorbed strontium, fits (within the noise of the data) were observed for both manganese and strontium in the second shell for all loadings and temperatures (Tables 1 and 3 and Fig. 5). Again, fits for Mn resulted in an average distance of approximately 4.12 Å and Sr at about 3.95 Å . In both cases, uncertainty in the coordination number decreased slightly with a decrease in temperature. To resolve the strontium sorption mechanism, we also collected Mn *K*-edge fluorescence data (Fig. 8). As seen in Fig. 9, the Fourier transformed spectra weighted with k^3 for HMO samples are presented; amplitudes and imaginary parts for the first two shells are equivalent for all samples. The first shell of oxygen atoms is located at about 1.89 Å, while the second shell of manganese atoms is at approximately 2.86 Å (Table 4, and a representative fit is shown in

TABLE 3

First (Oxygen)- and Second-Shell Best Fits for Sr *K*-Edge Data at 77, 200, and 298 K, *k*-Range 2.0 to 12.3 Å^{-1} and *r*-Range 1.1 to 4.0 Å

	Sample	Res. (%)	N_1	R_1 (Å)	σ_1^2 (Å^2)	$C_{3,1}$ (Å^3)	$C_{4,1}$
1.	4×10^{-3} mol Sr g^{-1} 77 K (Mn)[a]	1.43	12.13 ± 4.47	2.58 ± 0.065	0.011 ± 0.0087	$-2.7e\text{-}4 \pm 9.8e\text{-}4$	$-4.3e\text{-}5 \pm 2.4e\text{-}4$
2.	4×10^{-3} mol Sr g^{-1} 77 K (Sr)	1.31	12.33 ± 4.75	2.59 ± 0.065	0.012 ± 0.0092	$-1.4e\text{-}4 \pm 9.8e\text{-}4$	$-5.6e\text{-}5 \pm 2.5e\text{-}4$
3.	4×10^{-3} mol Sr g^{-1} 200 K (Mn)	1.82	11.35 ± 4.78	2.58 ± 0.077	0.013 ± 0.010	$-1.8e\text{-}4 \pm 1.2e\text{-}3$	$-8.3e\text{-}5 \pm 2.9e\text{-}4$
4.	4×10^{-3} mol Sr g^{-1} 200 K (Sr)	2.29	11.54 ± 4.86	2.59 ± 0.076	0.014 ± 0.010	$-1.4e\text{-}4 \pm 1.2e\text{-}3$	$-8.9e\text{-}5 \pm 2.8e\text{-}4$
5.	4×10^{-3} mol Sr g^{-1} 298 K (Mn)	2.27	10.93 ± 5.06	2.57 ± 0.080	0.016 ± 0.012	$-1.4e\text{-}4 \pm 1.3e\text{-}3$	$-1.5e\text{-}4 \pm 3.2e\text{-}4$
6.	4×10^{-3} mol Sr g^{-1} 298 K (Sr)	2.63	11.19 ± 5.12	2.58 ± 0.069	0.017 ± 0.011	$-3.0e\text{-}5 \pm 1.1e\text{-}3$	$-1.6e\text{-}4 \pm 3.0e\text{-}4$
7.	7×10^{-3} mol Sr g^{-1} 77 K (Mn)	1.34	12.66 ± 4.47	2.59 ± 0.062	0.013 ± 0.0083	$-1.8e\text{-}4 \pm 8.9e\text{-}4$	$-1.0e\text{-}4 \pm 2.2e\text{-}4$
8.	7×10^{-3} mol Sr g^{-1} 77 K (Sr)	1.56	12.97 ± 4.79	2.59 ± 0.060	0.014 ± 0.0086	$-1.4e\text{-}4 \pm 8.6e\text{-}4$	$-1.1e\text{-}4 \pm 2.2e\text{-}4$
9.	7×10^{-3} mol Sr g^{-1} 200 K (Mn)	1.72	11.91 ± 4.55	2.60 ± 0.065	0.015 ± 0.0093	$-1.5e\text{-}4 \pm 9.8e\text{-}4$	$-1.6e\text{-}4 \pm 2.4e\text{-}4$
10.	7×10^{-3} mol Sr g^{-1} 200 K (Sr)	2.00	12.30 ± 4.70	2.61 ± 0.062	0.016 ± 0.0091	$2.3e\text{-}4 \pm 9.1e\text{-}4$	$-1.8e\text{-}4 \pm 2.3e\text{-}4$
11.	7×10^{-3} mol Sr g^{-1} 298 K (Mn)	3.38	11.26 ± 5.58	2.56 ± 0.10	0.017 ± 0.013	$-3.9e\text{-}4 \pm 1.6e\text{-}3$	$-1.7e\text{-}4 \pm 3.6e\text{-}4$
12.	7×10^{-3} mol Sr g^{-1} 298 K (Sr)	3.77	12.18 ± 6.40	2.57 ± 0.095	0.019 ± 0.013	$-1.7e\text{-}4 \pm 1.5e\text{-}3$	$-2.2e\text{-}4 \pm 3.8e\text{-}4$
			N_2	R_2	σ_2^2	$C_{3,2}$	$C_{4,2}$
1.	4×10^{-3} mol Sr g^{-1} 77 K (Mn)[a]		2.20 ± 5.19	4.05 ± 0.085	0.013 ± 0.023	—	—
2.	4×10^{-3} mol Sr g^{-1} 77 K (Sr)		1.87 ± 15.11	3.96 ± 0.24	0.00093 ± 0.14	$1.7e\text{-}3 \pm 5.7e\text{-}3$	$4.2e\text{-}4 \pm 3.6e\text{-}3$
3.	4×10^{-3} mol Sr g^{-1} 200 K (Mn)		2.08 ± 12.31	4.13 ± 0.26	0.012 ± 0.12	$2.5e\text{-}3 \pm 6.7e\text{-}3$	$9.6e\text{-}5 \pm 3.4e\text{-}3$
4.	4×10^{-3} mol Sr g^{-1} 200 K (Sr)		3.51 ± 13.89	3.89 ± 0.11	0.019 ± 0.035	—	—
5.	4×10^{-3} mol Sr g^{-1} 298 K (Mn)		1.52 ± 7.16	4.11 ± 0.19	0.0096 ± 0.078	$2.1e\text{-}3 \pm 3.6e\text{-}3$	$-1.1e\text{-}5 \pm 1.7e\text{-}3$
6.	4×10^{-3} mol Sr g^{-1} 298 K (Sr)		1.89 ± 13.88	3.93 ± 0.23	0.0089 ± 0.11	$1.2e\text{-}3 \pm 4.6e\text{-}3$	$1.0e\text{-}4 \pm 2.4e\text{-}3$
7.	7×10^{-3} mol Sr g^{-1} 77 K (Mn)		2.02 ± 9.55	4.13 ± 0.20	0.0095 ± 0.093	$2.3e\text{-}3 \pm 4.8e\text{-}3$	$1.0e\text{-}4 \pm 2.4e\text{-}3$
8.	7×10^{-3} mol Sr g^{-1} 77 K (Sr)		3.55 ± 24.58	3.96 ± 0.24	0.010 ± 0.13	$2.0e\text{-}3 \pm 6.0e\text{-}3$	$2.6e\text{-}4 \pm 3.5e\text{-}3$
9.	7×10^{-3} mol Sr g^{-1} 200 K (Mn)		2.91 ± 13.03	4.15 ± 0.19	0.022 ± 0.08	$2.5e\text{-}3 \pm 3.6e\text{-}3$	$-2.6e\text{-}4 \pm 1.8e\text{-}3$
10.	7×10^{-3} mol Sr g^{-1} 200 K (Sr)		4.78 ± 27.61	3.98 ± 0.23	0.024 ± 0.098	$1.8e\text{-}3 \pm 5.0e\text{-}3$	$-1.6e\text{-}4 \pm 2.2e\text{-}3$
11.	7×10^{-3} mol Sr g^{-1} 298 K (Mn)		5.46 ± 21.66	4.14 ± 0.22	0.034 ± 0.073	$3.2e\text{-}3 \pm 3.7e\text{-}3$	$-5.2e\text{-}4 \pm 1.5e\text{-}3$
12.	7×10^{-3} mol Sr g^{-1} 298 K (Sr)		12.30 ± 56.20	4.00 ± 0.21	0.044 ± 0.07	$3.0e\text{-}3 \pm 2.9e\text{-}3$	$-6.6e\text{-}4 \pm 1.4e\text{-}3$

[a] (Mn) or (Sr) represents the second-shell atom used in the model.

Fig. 5). The ratio of coordination numbers for these two shells is about 1:1 (absolute values for each shell could not be determined because the structure is unknown and therefore self absorption corrections were not possible). There is no evidence of strontium in the second shell. In addition, the XANES region for manganese was assessed to determine whether the site symmetry for the Mn environment in the microcrystalline, amorphous manganese oxide changed as a function of strontium loading or manganese oxide aging (Fig. 10). These results indicate that the Mn environment in the HMO remains intact as a discrete oxide and that neither a solid solution nor a crystalline oxide of Mn–Sr forms. Furthermore, although amorphous, this oxide exhibits a highly ordered local structure. The XANES and XAFS data (Fig. 5) are also in agreement with the X-ray diffraction patterns discussed earlier. Axe and Anderson (13) observed similar results with both aged HFO and strontium sorbed to HFO, as there was no macroscopic change in the ferrihydrite. Specifically, they showed that no other type of oxide such as an iron–strontium oxide precipitate formed, including a discrete-phase strontium carbonate.

TABLE 4

First (Oxygen)- and Second (Manganese)-Shell Best Fits for Mn *K*-Edge Data, *k*-Range 2.15 to 11.0 Å^{-1} and *r*-Range 1.08 to 3.08 Å

Sample	R	N_1[a]	R_1 (Å)	σ_1^2 (Å^2)	N_2[a]	R_2 (Å)	σ_2^2 (Å^2)
HMO	1.64	3.61 ± 0.74	$1.89 \pm 9.66 \times 10^{-3}$	$1.91 \times 10^{-3} \pm 1.82 \times 10^{-3}$	3.12 ± 0.95	$2.86 \pm 1.23 \times 10^{-2}$	$3.44 \times 10^{-3} \pm 2.28 \times 10^{-3}$
HMO 0.1 mmol Sr/g	1.43	3.96 ± 0.73	$1.89 \pm 8.76 \times 10^{-3}$	$1.76 \times 10^{-3} \pm 1.64 \times 10^{-3}$	3.34 ± 0.91	$2.86 \pm 1.13 \times 10^{-2}$	$3.02 \times 10^{-3} \pm 2.03 \times 10^{-3}$
HMO 1 mmol Sr/g	2.04	3.82 ± 0.75	$1.89 \pm 9.56 \times 10^{-3}$	$2.19 \times 10^{-3} \pm 1.78 \times 10^{-3}$	3.27 ± 0.98	$2.86 \pm 1.22 \times 10^{-2}$	$3.68 \times 10^{-3} \pm 2.26 \times 10^{-3}$
HMO 4 mmol Sr/g	1.04	3.84 ± 0.71	$1.89 \pm 8.60 \times 10^{-3}$	$1.36 \times 10^{-3} \pm 1.60 \times 10^{-3}$	3.48 ± 0.97	$2.87 \pm 1.15 \times 10^{-2}$	$3.61 \times 10^{-3} \pm 2.11 \times 10^{-3}$
HMO 7 mmol Sr/g	1.52	3.94 ± 0.73	$1.89 \pm 8.87 \times 10^{-3}$	$1.85 \times 10^{-3} \pm 1.66 \times 10^{-3}$	3.53 ± 0.98	$2.86 \pm 1.16 \times 10^{-2}$	$3.69 \times 10^{-3} \pm 2.09 \times 10^{-3}$
HMO 10 mmol Sr/g	1.73	3.64 ± 0.74	$1.89 \pm 9.66 \times 10^{-3}$	$1.92 \times 10^{-3} \pm 1.81 \times 10^{-3}$	3.14 ± 0.95	$2.87 \pm 1.24 \times 10^{-2}$	$3.40 \times 10^{-3} \pm 2.28 \times 10^{-3}$
HMO 10 mmol Sr/g aged 6 months	1.94	3.60 ± 0.76	$1.89 \pm 1.03 \times 10^{-2}$	$2.31 \times 10^{-3} \pm 1.92 \times 10^{-3}$	3.15 ± 0.99	$2.87 \pm 1.32 \times 10^{-2}$	$3.76 \times 10^{-3} \pm 2.39 \times 10^{-3}$
HMO aged 6 months	0.87	3.37 ± 0.76	$1.89 \pm 1.11 \times 10^{-3}$	$2.37 \times 10^{-3} \pm 2.06 \times 10^{-3}$	2.86 ± 1.40	$2.86 \pm 1.40 \times 10^{-2}$	$3.46 \times 10^{-3} \pm 2.49 \times 10^{-3}$

[a] Because the structure is not known, self-absorption corrections to the amplitude of the XAFS data were not possible. Consequently, only relative coordination numbers are correct and not absolute values.

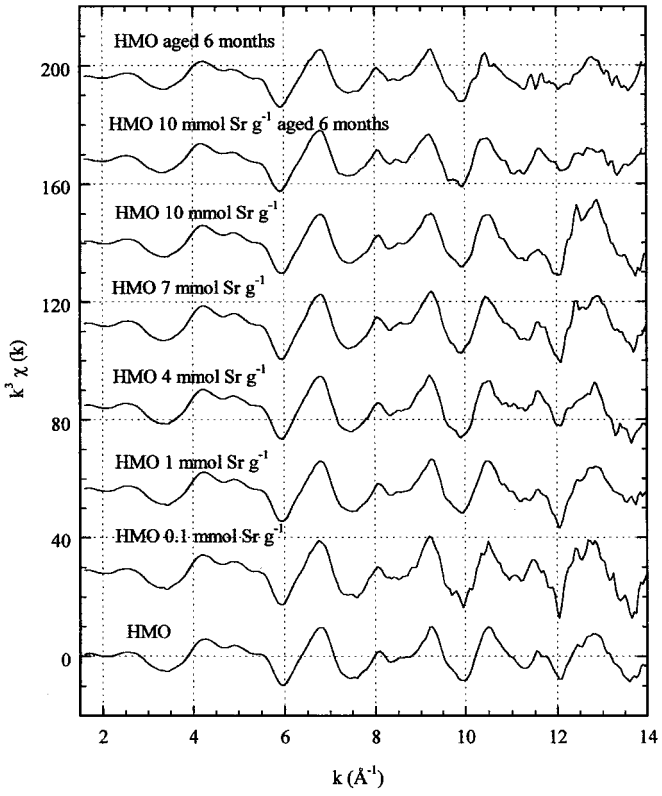

FIG. 8. Mn K-edge data reduced to $\chi(k) \cdot k^3$ versus k.

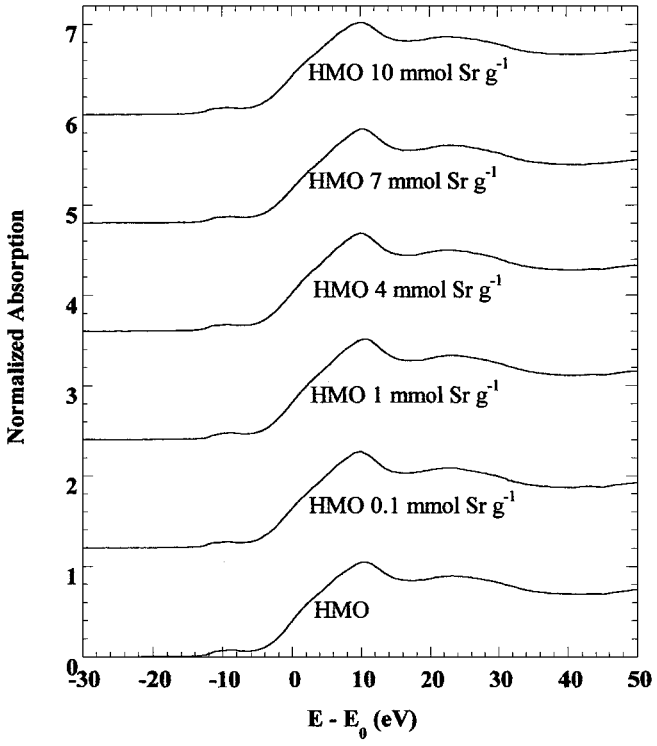

FIG. 10. Mn K-edge data of −30 to 50 eV from edge.

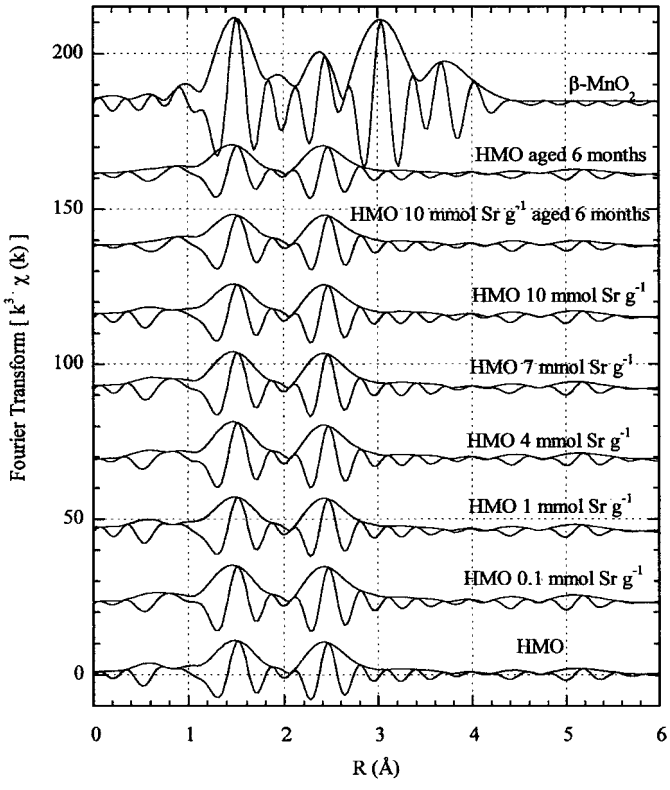

FIG. 9. Fourier transform $[k^3 \cdot \chi(k)]$ versus radial coordinate filtered from 2.15 to 11.0 Å^{-1}.

CONCLUSIONS

The XAS results assisted in delineating the mechanistic model for strontium sorption to the hydrous manganese oxide surface as a function of loading. In distinguishing physical sorption from chemical sorption, the coordination environment would suggest that the waters of hydration around the strontium ion remain as the ion complexes with the HMO surface. Because Sr adsorbs through physical forces, the fraction sorbed to the external surface is available for partitioning with the aqueous phase. However, because hydrous manganese oxides like those of aluminum and iron are microporous, contaminants like Sr 90 may slowly diffuse in these pores (11–15, 34). In isotherm studies, Trivedi and Axe (34) observed one average type of site on the HMO surface. Because there is no evidence that external and internal surface sites are different, local structure from short-term studies should be the same as that in the long-term ones. The oxide acts not only as a sink but also as a source, which is not accounted for in most hydrogeochemical models. Although metastable, these oxides may be stable in aquatic environments as HMO was observed to be stable up to 6 months with or without the strontium, suggesting that this oxide maintains its sorption capacity in aqueous environments.

ACKNOWLEDGMENT

This research was supported by NSF Grant BES-9753072.

REFERENCES

1. Manceau, A., Gorshkov, A. I., and Drits, V. A., *Am. Mineral.* **77,** 1133–1143 (1992).
2. Manceau, A., Gorshkov, A. I., and Drits, V. A., *Am. Mineral.* **77,** 1144–1157 (1992).
3. Manceau, A., Chalet, L., Boisset, M. C., Didier, B., and Spadini, L., *Appl. Clay Sci.* **7,** 201 (1992).
4. Waychunas, G. A., Rea, B. A., Fuller, C. C., and Davis, J. A., *Geochim. Cosmochim. Acta* **57,** 2251–2269 (1993).
5. Manceau, A., Boisset, M. C., Sarret, G., Hazemann, J. L., Mench, M., Cambier, P., and Prost, R., *Environ. Sci. Technol.* **30,** 1540–1552 (1996).
6. Friedl G., Wehrli, B., and Manceau, A., *Geochim. Cosmochim. Acta* **61,** 275–290 (1997).
7. Axe, L., Bunker, G. B., Anderson, P. R., and Tyson, T. A., *J. Colloid Interface Sci.* **199,** 44–52 (1998).
8. Bargar, J. R., Brown, G. E., and Parks, G. A., *Geochim. Cosmochim. Acta* **61,** 13, 2617–2637 (1997).
9. Bargar, J. R., Brown, G. E., and Parks, G. A., *Geochim. Cosmochim. Acta* **61,** 13, 2639–2652 (1997).
10. Bargar, J. R., Brown, G. E., and Parks, G. A. *Geochim. Cosmochim. Acta* **62,** 2, 193–207 (1998).
11. Strawn, D. G., Scheidegger, A. M., and Sparks, D. L., *Environ. Sci. Technol.* **32,** 17, 2596–2601 (1998).
12. Fuller, C. C., Davis, J. A., and Waychunas, G. A., *Geochim. Cosmochim. Acta* **57,** 2271–2282 (1993).
13. Axe, L., and Anderson, P. R., *J. Colloid Interface Sci.* **175,** 1, 157–165 (1995).
14. Papelis, C., Roberts, P. V., and Leckie, J. O., *Environ. Sci. Technol.* **29,** 4, 1099–1108 (1995).
15. Axe, L., and Anderson, P. R., *J. Colloid Interface Sci.* **185,** 436–448 (1997).
16. Bunker, G., *Nucl. Instrum. Methods* **207,** 437 (1983).
17. Dalba, G., and Fornasini, P., *Phys. Rev. B* **47,** 8502 (1993).
18. Collins, C. R., Sherman, D. M., and Ragnarsdóttir, K. V., *Radiochim. Acta* **81,** 201–206 (1998).
19. Chen, C. C., Papelis, C., and Hayes, K. F., *in* "Adsorption of Metals by Geomedia" (E. A. Jenne, Ed.), Chap. 15. Academic Press, New York, 1998.
20. Parkman, R. H., Charnock, J. M., Livens, F. R., and Vaughan, D. J., *Geochim. Cosmochim. Acta* **62**(9), 1481–1492 (1998).
21. Manceau, A., and Charlet, L., *J. Colloid Interface Sci.* **148**(2), 425–442 (1992).
22. Charlet, L., and Manceau, A., *J. Colloid Interface Sci.* **148**(2), 443–458 (1992).
23. Manceau, A., and Charlet, L., *J. Colloid Interface Sci.* **168,** 87–93 (1994).
24. Spadini, L., Manceau, A., Schindler, P.W., and Charlet, L., *J. Colloid Interface Sci.* **168,** 73–86 (1994).
25. Gadde, R. R., and Laitinen, H. A., *Anal. Chem.* **46,** 13 (1974).
26. Allison, J. D., Brown, D. S., and Novo-Gradac, K. J., "MINTEQA2/PRODEFA2, A Geochemical Assessment Model for Environmental Systems: Version 3.0 User's Manual." Environmental Research Laboratory, Office of Research and Development, U.S. Environmental Protection Agency, Athens, Georgia, 1991.
27. Bouldin, C. E., Elam, W. T., and Furenlid, L., *Physica B* **208/209,** 190 (1995).
28. Bunker, B., Sayers, D., *in* "X-Ray Absorption: Principles, Applications, Techniques of EXAFS, SEXAFS, and XAFS" (D. C. Koningsberger and R. Prins, Eds.). Wiley, New York, 1988.
29. D'Angelo, P., and Nolting, H.-F., *Phys. Rev. A* **53**(2), 798–805 (1996).
30. Zabinsky, S. I., Rehr, J. J., Ankudinov, A., Albers, R. C., and Eller, M. J., *Phys. Rev. B* **52**(4), 2995–3009 (1995).
31. Morgan, J. J., and Stumm, W., *J. Colloid Interface Sci.* **19,** 347–359 (1964).
32. Hans, S., Anderson, F. J., and Walter, W. J., *Environ. Sci. Technol.* **12,** 1086–1091 (1968).
33. Murray, J. W., *J. Colloid Interface Sci.* **46,** 3 (1973).
34. Trivedi, P., and Axe, L., *J. Colloid Interface Sci.* **218,** 554–563 (1999).